

Suction side film cooling measurements in a linear high-temperature cascade at near-engine conditions

Original article

Article history:

Submission date: 4 November 2024 Acceptance date: 12 March 2025 Publication date: 17 November 2025



Check for updates

*Correspondence:

JL: lemmer@ist.rwth-aachen.de

Peer review:

Single blind

Copyright:

© 2025 Lemmer et al. @ This is an open access article distributed under the Creative Commons Attribution Non Commercial License (CC BY-NC 4.0), which permits unrestricted use, distribution, and reproduction in any medium for noncommercial purposes only, provided the original work is properly cited and its authors credited.

Kevwords:

film cooling; experiment; turbine cooling; high temperature

Citation

Lemmer J., Kleine-Hollenhorst Y., Dehe V., Jeschke P., and Rabs M. (2025). Suction side film cooling measurements in a linear high-temperature cascade at near-engine conditions. Journal of the Global Power and Propulsion Society. 9: 213–223. https://doi.org/10.33737/jgpps/202914

Jan Lemmer^{1,*}, Yanik Kleine-Hollenhorst¹, Viola Dehe¹, Peter Jeschke¹, Michael Rabs²

¹Institute of Jet Propulsion and Turbomachinery, RWTH Aachen University, Templergraben 55, 52062 Aachen, Germany

²MAN Energy Solutions SE, Steinbrinkstraße 1, 46145 Oberhausen, Germany

Abstract

Film-cooled turbine blades in a Linear High-Temperature Cascade are investigated experimentally and numerically at a Reynolds number of 120,000, low inlet Mach numbers (Ma = 0.2), and main flow temperatures of up to 1,050 K. Variations in cooling air temperature are used to achieve different density ratios. In addition, the cooling air mass flow is varied for different coolant mass flow ratios. The blades are derived from the midsection of a high-pressure turbine blade and feature a single row of film cooling holes on the suction side. They are equipped with 66 thermocouples and 37 pressure taps. Film cooling reduces the material temperature in the region downstream of the holes up to 65% of the chord length. High mass ratios of MR > 1.0% result in a reversal of the cooling effect due to the detachment of the cooling film. In summary, we provide temperature and pressure measurements of a film-cooled turbine blade at realistic density and mass flow ratios utilizing a unique linear cascade supplied with high-temperature exhaust gas flow. Our paper contributes to the validation of numerical codes used for the thermal design of turbine blades.

Introduction

Film cooling is a method which is essential in gas turbine engines to mitigate the adverse effects of high temperatures on turbine components. This improves the thermal efficiency of the engine and durability. Understanding the complex aerodynamic and thermal phenomena associated with film cooling is critical for advancing turbine design and optimization. Despite the extensive research conducted over the last 50 years, including fundamental work such as Goldstein's (1971), a complete understanding of the flow physics remains elusive, primarily due to the large number of influencing factors, such as geometric configurations and flow parameters.

Many studies focus on flat plates and low temperatures (<600 K) in order to use sophisticated measurement techniques, such as thermography (Baldauf et al., 1999) or pressure sensitive paint (Narzary et al., 2011) to measure the local heat transfer coefficient h and an adiabatic film cooling effectiveness η . Scaling these results to turbine blades or vanes under engine conditions faces many challenges, for example a different gas composition (Rutledge et al., 2016) and mismatched dimensionless groups (Ornano and Povey, 2020). In addition, scaling from a flat plate to a blade or vane leads to incorrect predictions of the cooling performance (Bacci et al., 2019). Experimental investigations are therefore essential to improve film cooling strategies by elucidating complex



flow physics and validating computational models. This study focuses on suction side film cooling measurements conducted in a Linear High-Temperature Cascade under conditions closely resembling those encountered in actual engine environments.

Very few test rigs are currently able to generate comparable test conditions. In the 1980s, turbine blade measurements were carried out at temperatures of up to 811 K at the Aerothermodynamic Cascade Facility of the Allison Engine Company (Hylton et al., 1983; Nealy et al., 1984). Static pressure taps, Laser Doppler Anemometry (LDA), and hot-wire measurements were used to measure Mark II and C3X profiles in a cascade consisting of three guide vanes. Thermocouples were mounted on the outside and the local heat transfer coefficients were determined numerically according to Turner (1971). The Hachinohe Institute of Technology in Japan operates a cascade test rig for stator and rotor blades (Okamura et al., 2003). The combustion of hydrogen and oxygen reaches temperatures of up to 1,973 K at a pressure of 2.5 MPa. Thermocouples and pressure taps are installed in the blades, in addition to pressure and temperature measurements being taken at the inlet. ABB STAL in Sweden developed a pressurized test rig to analyze real turbine blades at temperatures of up to 1,170 K (Rådeklint and Hjalmarsson, 1998; Rubensdörffer and Hjalmarsson, 1998). Infrared thermography can be used to measure surface temperature distributions on the leading edge of the blade, on the front part of the pressure side, and on a downstream part of the suction side, through optical access. Additional high-temperature measurements in an exhaust gas environment, reaching temperatures of up to 1,423 K, were conducted by (Ramesh et al., 2014) using cylindrical film cooling holes on a flat plate.

Methodology

Experimental setup

The Linear High-Temperature Cascade (LHTC) at the Institute of Jet Propulsion and Turbomachinery is a test rig designed to test cooled turbine blades at high temperatures and realistic density ratios (Findeisen et al., 2017). Currently, the rig is being used to test and validate film-cooled turbine blades as part of a research project. The rig can operate at main flow temperatures of up to 1,300 K and hot gas mass flows of up to 1.2 kg/s, generated by an engine combustion chamber. Figure 1 shows the cross section of the LHTC, which comprises five turbine blades. The main stream air flow is supplied by a compressor with up to 5 kg/s. A dieselfueled combustion chamber heats the main flow to up to 1,300 K. The test rig has two flow paths downstream of the flame tube. The bypass flow serves as a cooling system for the inner hot gas ducts and ensures thermal decoupling of the outer housing. Three traversable, water-cooled total temperature and total pressure probes are located in the straight section downstream of the transition duct. These are used to measure a two-dimensional flow inlet profile. Three static pressure taps are installed upstream of the probes. These measurements allow the operating point to be characterized. Due to the high temperatures and locally varying concentrations of exhaust gas, the transport and material properties of the flow differ noticeably from those of dry air. Hence, they are calculated for every measurement point using Cantera (Goodwin et al., 2023) and a diesel surrogate fuel model

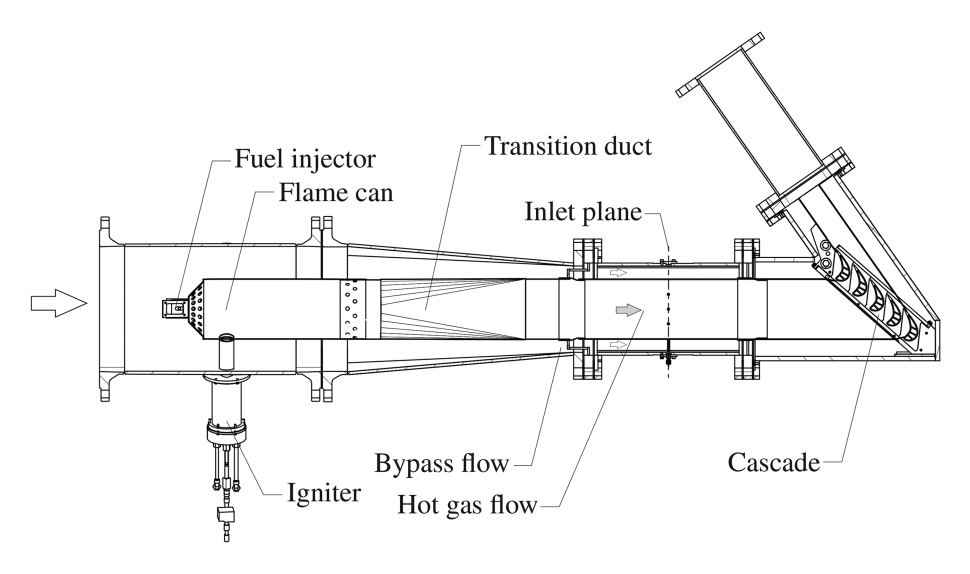


Figure 1. Section View of the Linear High-Temperature Cascade.

(Pei et al., 2015). On this basis, the mass flow $\dot{m}_{\rm HG}$ of the hot gas flow and a mass flow averaged operating point can be calculated. The flow is characterized by the Reynolds number in the hot gas flow

$$Re_{HG} = \frac{\dot{m}_{HG}L}{A\mu},\tag{1}$$

where L is the chord length, A the cross section area of the inlet section and μ the dynamic viscosity. The latter is also calculated with Cantera on the basis of the calculated flow conditions. All the results presented were obtained at Re_{HG} $\approx 120 \times 10^3$.

Blade configuration and instrumentation

The cascade is comprised of five blades, of which the outer blades form the wall for the hot air flow, while the three blades in the middle of the cascade are used for temperature (middle blade) and pressure measurements (adjacent blades), cf. Figure 2. The blade cooling design is derived from the mid-section of a high-pressure turbine blade and features four smooth internal cooling channels. The three middle blades each have 18 cylindrical film cooling holes which are located on the suction side of the first channel. To ensure mass conservation in the fourth channel, trailing edge ejection is not utilized. The blades are mounted in the test rig with the tip plates facing downwards. The middle blade is equipped with a total of 66 thermocouples to measure the metal temperature of the blade. Of these, 32 thermocouples are located in the mid-plane, while 16 thermocouples are located in both the hub and tip planes at 10% and 90% of the blade height respectively.

The blades to the left and right of the center are used for measuring the profile pressure at a total of 37 pressure taps. Based on the profile pressure the isentropic Mach number

$$Ma_{is} = \sqrt{\frac{2}{\kappa - 1} \left[\left(\frac{p_{t, HG}}{p} \right)^{((\kappa - 1)/\kappa)} - 1 \right]}$$
 (2)

is calculated, where p_{pHG} is the main flow total pressure at the inlet plane and κ the isentropic exponent of the main flow exhaust gas. Additionally, 34 pressure taps are located at the tip plate (cf. Figure 2) to measure the static pressure at the cascade inlet and outlet as well as in the passage between the blades.

Blade cooling

The cooling air is provided by a separate compressor and can be heated by a flow heater to up to 573 K. A total of six valves are used to control the mass flow to the blades. Figure 3 shows the cooling air supply and tubing for the central blade. Air is supplied to the entrance of channels 1 and 2 from the flow heater. Instead of using the usual internal deflection, the cooling air is guided out of the blade and deflected to a pipe section before entering the next cooling channel. After passing channel 1, the cooling air is blown out into the bypass flow. The cooling air from channel 2 is guided through pipes outside the blade and redirected into the following channels 3 and 4. Downstream of channel 4, the cooling air is blown out into the bypass.

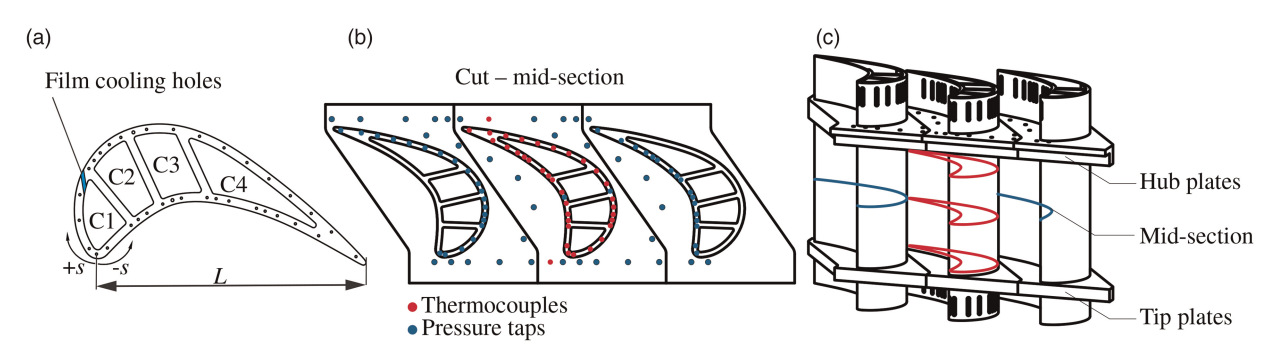


Figure 2. Test blades with measurement locations. (a) Mid-section of the tested blade showing the cooling channels and the location of the film cooling row with 18 cylindrical film cooling holes at $s/L \approx 0.35$. (b) Top view, (c) Side view of the three middle blades. The middle blade is equipped with thermocouples, while the adjacent blades have holes for profile pressure measurements.

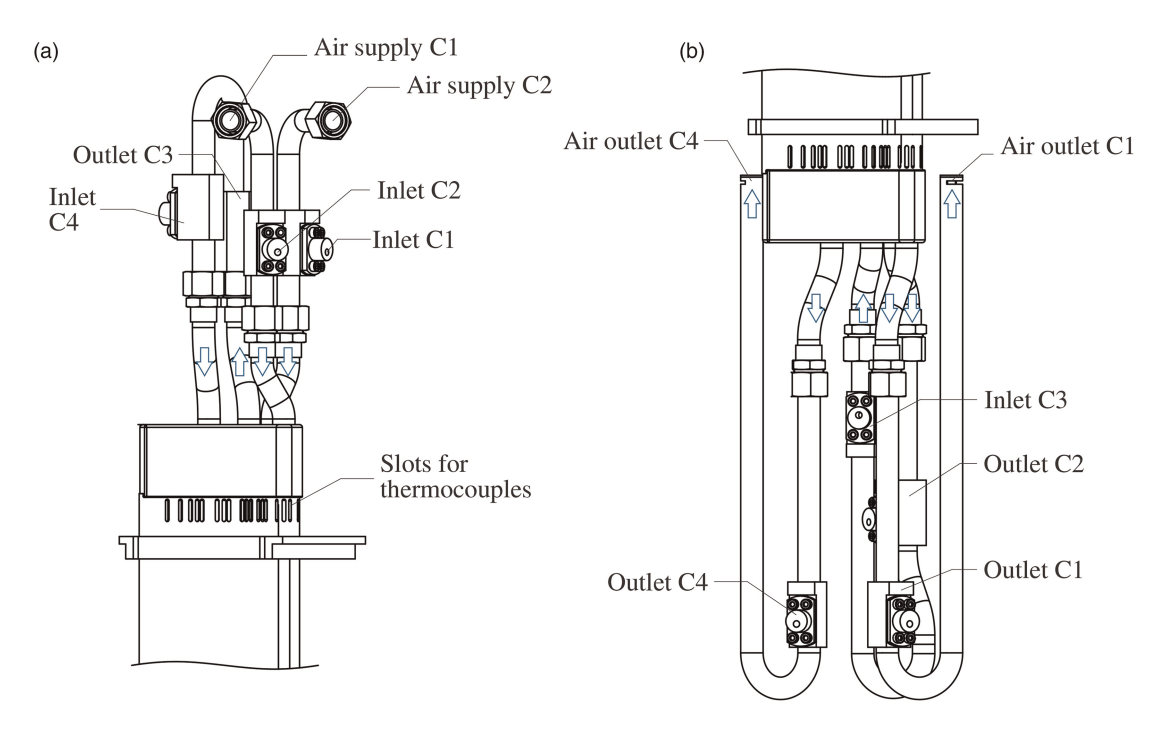


Figure 3. External cooling air pipes of the central measurement blade, (a) top side and (b) bottom side of the blade. Static pressure, total pressure and temperature are measured at each channel inlet and outlet.

To characterize the cooling air flow, cooling air measurement sections (CAM) are used. Six CAMs are placed at the cooling air inlets of the three middle blades, so that each inlet is measured separately. Six more CAMs are placed in the external cooling air path of the middle blade (cf. Figure 3), so that there is one measurement section upstream and downstream of each channel respectively. This enables the measurement of inlet and outlet quantities at each of the four cooling air channels of the center blade. These values serve as boundary conditions for CFD calculations of the blade.

Each CAM contains a combined Kiel head probe for total pressure and total temperature measurements (cf. Findeisen et al., 2017). Additionally, three pneumatically averaged static pressure taps are located upstream of the Kiel probe to determine the Mach number, which is used for recovery factor correction of the total temperature probe. The coolant mass flow \dot{m}_C can be calculated on the basis of values for total pressure, temperature and static pressure. Due to the existence of boundary layers and inhomogeneous velocity profiles, every CAM is calibrated in-situ with an EN ISO 5167-2 compliant measurement orifice. With this calibration the uncertainty of the CAM mass flow is approximately 0.9×10^{-3} kg/s, which depends slightly on the coolant temperature and total pressure.

The operating point of the cooling air is determined by the combination of coolant temperature T_C and the coolant mass flow \dot{m}_C . We use the ratio of the density of the coolant fluid to that of the main flow $\mathrm{DR} = \rho_C/\rho_{\mathrm{HG}}$ as a similarity parameter. For the first channel, where the film cooling holes are located, the ratio of film cooling to main stream mass flow is used

$$MR = \frac{\dot{m}_C}{\dot{m}_{HG}} = \frac{\dot{m}_{C1,in} - \dot{m}_{C1,out}}{\dot{m}_{HG}}.$$
 (3)

The film cooling mass flow \dot{m}_C is the difference between the inlet $\dot{m}_{C1,\text{in}}$ and outlet mass flow $\dot{m}_{C1,\text{out}}$ of channel 1. When MR is changed, the mass flow in channel 2 is set equal to the mass flow of channel 1 $\dot{m}_{C1,\text{in}} = \dot{m}_{C2,\text{in}}$. To characterize the convective cooling the total coolant to main stream ratio

$$TCR = \frac{\dot{m}_{C, \text{tot}}}{\dot{m}_{HG}} \tag{4}$$

is used, where $\dot{m}_{C,\text{tot}}$ is the sum of the inlet mass flow of channel 1 and 2.

Numerical setup

Steady-state conjugate heat transfer (CHT) simulations were performed to analyze both the aerodynamic characteristics and the thermal conditions of the blades. The numerical setup shown in Figure 4 is composed of the hot gas domain, the cooling air domain and the solid blade domain. Separate computational meshes were created for each domain using Ansys ICEM CFD. Ansys CFX was used for all steady-state simulations. The hot gas domain featured only one passage of the test rig with periodic boundaries in pitchwise direction. At the inlet, total temperature and total pressure profiles from the inlet probes were used. Since there is no pressure measurement downstream of the cascade, the outlet static pressure was adjusted to match the blade surface pressure distribution of the experimental data. The hot gas was modeled as an exhaust gas consisting of N₂, O₂, CO₂ and H₂O with temperature-dependent fluid properties. For the cooling air domain, the cooling air pipes were split at each CAM. In this way, the inlet (total temperature and total pressure) and outlet (static pressure) boundary conditions can be directly adopted from the respective experimental CAM data. The cooling air was modeled as dry air consisting of N₂ and O₂ with temperature-dependent fluid properties. The first cooling channel featured a fluid-fluid interface with respect to the hot gas flow, allowing the cooling air to pass through the film cooling holes into the main stream.

The solid domain is placed between the hot gas and the cooling air. The thermal conductivity of the solid matches the properties of Alloy X. Fluid-solid interfaces are defined on the walls adjacent to the hot gas or cooling air flow respectively. All walls located within the bypass are almost adiabatic due to the thermal insulation in the test rig.

All simulations were carried out using both the k- ω -SST turbulence model (Menter, 1994) and the BSL EARSM (Wallin and Johansson, 2000), each in combination with the γ -Re $_{\theta}$ transition model (Menter et al., 2006). Since the results of the BSL EARSM model were in better agreement with the experimental data, only these results are presented here. Three different levels of mesh refinement were investigated and differences in the film cooling region were observed across all mesh levels. A finer mesh was not considered due to excessive computational cost. Consequently, the finest mesh was selected for the simulations. This mesh contains a 60 million elements structured mesh for the hot gas domain to accurately resolve the film cooling flow entering the hot gas flow and a 40 million elements unstructured mesh for the cooling air channels. As a result, an average non-dimensional wall distance of $y^+ = 0.3$ was achieved in the fluid parts. Additionally, an unstructured grid of 10 million elements was created for the solid blade.

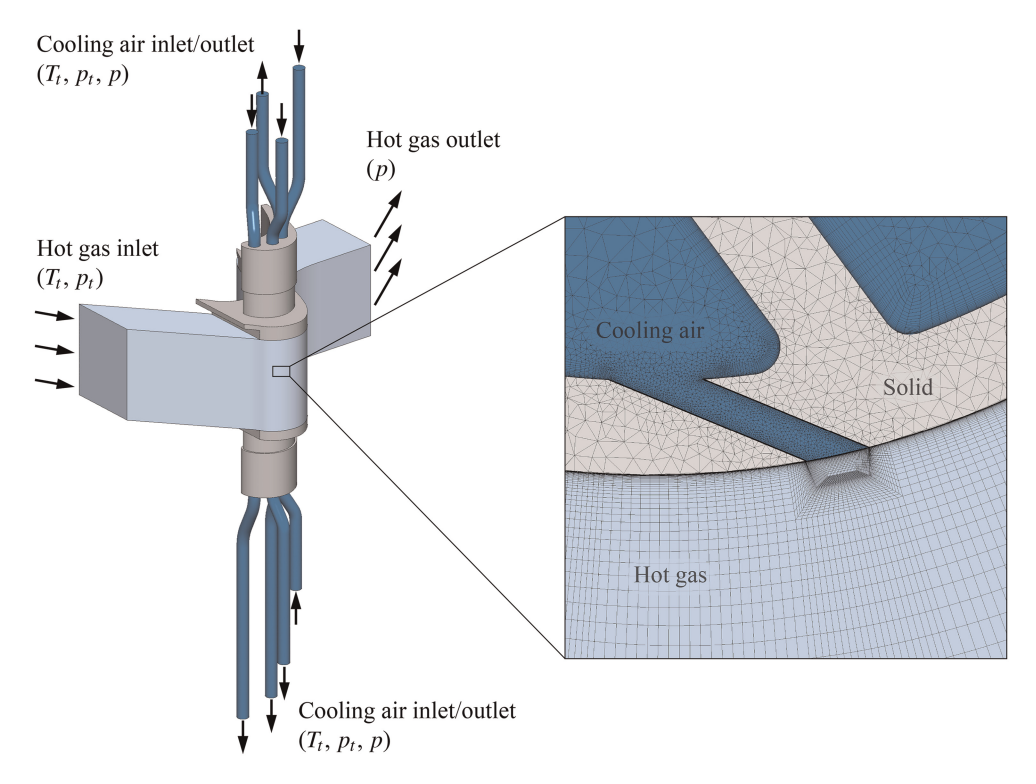


Figure 4. Computational domain and mesh used for CFD simulations.

Based on the simulation results, the momentum ratio I of the film cooling flow can be calculated

$$I := \frac{(\rho c^2)_C}{(\rho c^2)_{HG}} \tag{5}$$

$$(\rho c^2)_{HG} = \frac{p}{RT} a^2 M a_{is}^2 = \frac{p}{RT} \kappa R T M a_{is}^2 = p \kappa M a_{is}^2.$$
 (6)

The momentum of the main flow $(\rho c^2)_{HG}$ is calculated using the pressure and the isentropic Mach number (Equation 2) at the film cooling row. It is important to note that the momentum ratio cannot be measured in the experiment.

Results and discussion

In this section, we first present the measurements of the inlet plane, which serve as inlet boundary conditions for the simulation. Next, we provide the experimental results obtained for a main stream temperature of $T \approx 1,050 \text{ K}$ and $\text{Re} = 120 \times 10^3$, which form the basis for validation and subsequent discussion. An overview of the experimental operating points is given in Table 1. Finally, we use CFD to separate film cooling and internal cooling effects with the aim of gaining for a more comprehensive understanding of the data presented.

Inlet conditions

The inlet profile of the main flow for the following results is shown in Figure 5. The temperature profile at the inlet shows a significant gradient in the vertical direction (z), with temperature peaks located above the channel mid-plane. A thermal boundary layer is visible near the hub. The total pressure near the tip is significantly lower than at the hub, which can be explained by the interaction between the rotation-symmetric temperature profile generated by the fuel nozzle of the flame can and the liner. The transition duct changes the circular cross-section of the combustor the rectangular shape of the inlet section. This transition involves a reduction in channel height to half the diameter of the combustor section, while maintaining a consistent channel width, which results in the following two effects. First, the rotation-symmetric temperature profile contracts vertically. Second, the resulting non-uniform flow acceleration induces a secondary flow that transports cold fluid from the near wall towards the hot gas mid-plane (Mick et al., 2013). These overlapping effects explain the observed total temperature and pressure profile, which remains consistent for all operating points.

Validation of the CFD results

CFD simulations were used to get a more detailed view of the flow field and the heat transfer of the blade. A comparison between the experimental data and the numerical results is shown in Figure 6. The left-hand diagram illustrates the isentropic Mach number Ma_{is} in the mid-plane of the blades. In the right-hand diagram the normalized blade material temperature is shown for two different mass flow ratios. Overall, the numerical results are in good agreement with the measured material temperatures. However, downstream the film cooling row the CFD simulations overestimate the material temperatures on the suction side from s/L > 0.8.

Table 1. Experimental operating points.

ОР	Re _{HG}	$T_{t, HG}$	DR	MR	TCR ^a	l _p
1	120 × 10 ³	1,050 K	2.3	0.6%	4.9%	_
2	120 × 10 ³	1,050 K	2.5	0.5, 0.6, 0.8, 1.2%	3.7, 4.9, 5.9, 10%	0.4, 0.7, 1.1, 2.7
3	120 × 10 ³	1,050 K	3.0	0.6%	4.9%	_

OP2 is used for the CFD simulations.

^aTCR results from MR and the condition of equal mass flow in C1 and C2.

^bMomentum ratio is calculated on the basis of the simulations.

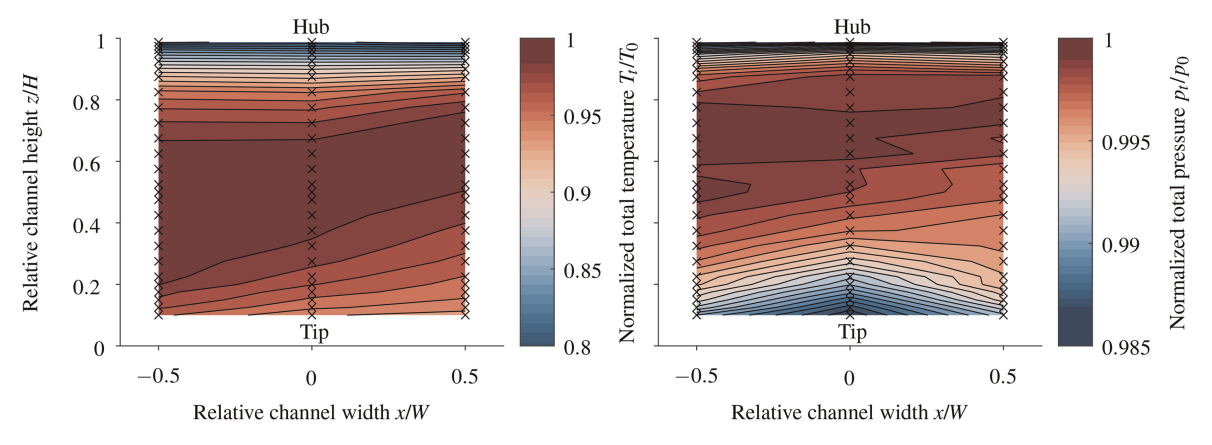


Figure 5. Normalized total pressure and temperature profile at the inlet section for $Re_{HG} = 120 \times 10^3$. Each cross is a measurement point, values in between are linear interpolations.

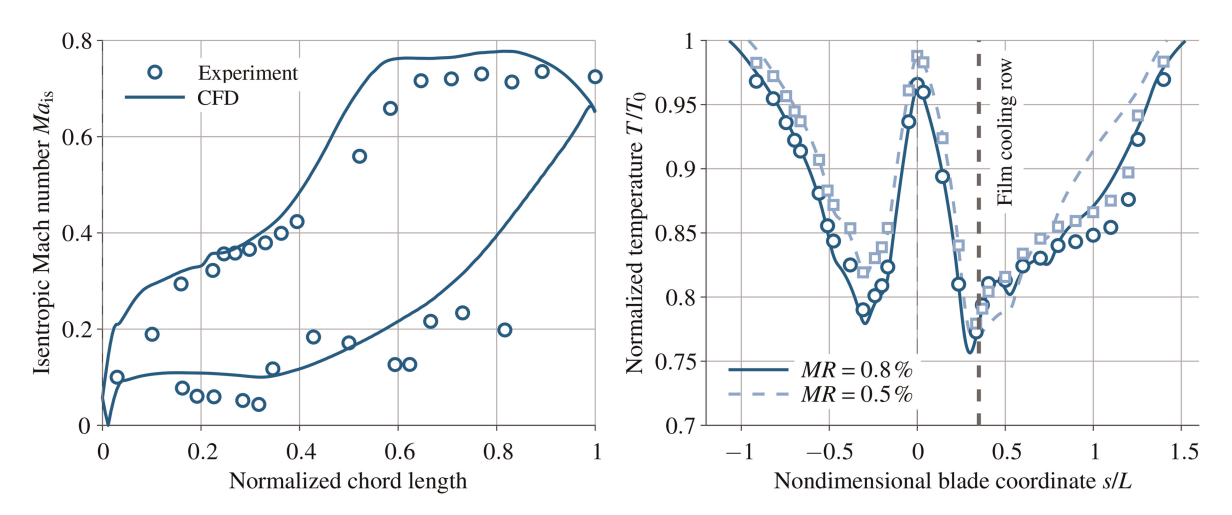


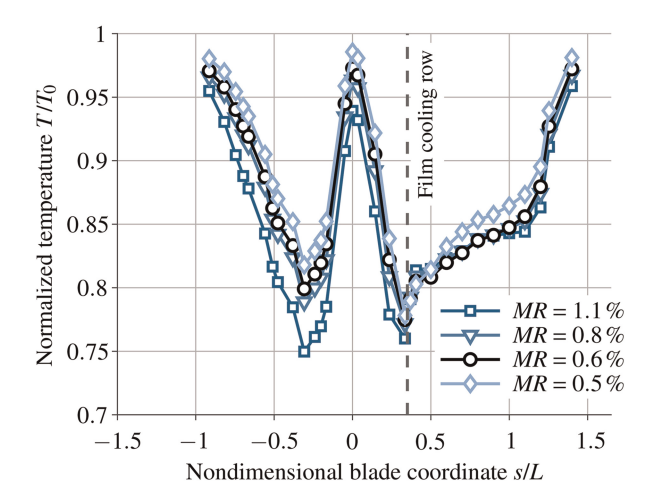
Figure 6. Comparison between the experimental data and the CFD simulations for OP2. Left: isentropic Mach number. Right: blade material temperature.

Experimental results

Effect of varying coolant mass flow ratio

Figure 7 shows on the left-hand side the normalized blade temperature of the film-cooled blade for four different mass flow ratios. As the coolant mass flow increases, the material temperature generally decreases due to the higher overall cooling air flow. This effect is particularly noticeable on the pressure side which is only convectively cooled and on the suction side upstream of the film cooling row. The design of the blade causes film cooling and convective cooling to interact. A high film cooling mass flow requires high pressure in the cooling channels due to the significant pressure loss at the exit of the film cooling holes. However, the pressure resistance for the internal cooling flow, which determines the mass flow, remains almost constant. The total mass flow therefore increases disproportionately when MR is increased. For instance, an MR of 1.1% leads to a TCR that is twice as high as for MR = 0.8%. However, when MR is low, TCR also decreases, resulting in a lower absolute heat flow in channel 2-4 and an increase in material temperature.

Downstream of the film cooling holes s/L > 0.35, an increase in film cooling mass flow does not result in a reduction in the material temperature. Only at very low mass flow ratios of 0.5%, does the blade temperature increase due to the reduced total mass flow. Directly behind the film cooling holes $s/L \approx 0.4$, the temperature actually increases as the cooling mass flow increases. This is most likely due to the separation of the cooling jet, which drastically reduces the film cooling effectiveness downstream of the film cooling row. This effect is then compensated for by the increased convective cooling further downstream on the blade.



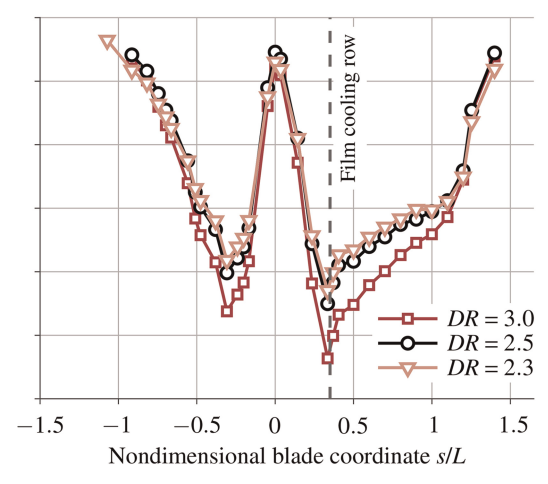


Figure 7. Normalized material temperature at the mid-section plan for different coolant mass ratios MR left and for different coolant density ratios DR right. The black colored graph shows the same operating point in both diagrams.

Effect of varying density ratio

In the right-hand diagram of Figure 7, the coolant mass flow ratio is held constant (MR = 0.6%), while different density ratios between 2.3 and 3 are compared. The leading edge temperature is insensitive to different density ratios. On both the pressure side and the suction side the temperature decreases with higher density ratio. This is because an increasing density ratio means a lower coolant temperature and a higher coolant Reynolds number, leading to a better internal cooling of the blade. The suction side especially, is very sensitive to changes in density ratio. In addition to the abovementioned effects, the film cooling effectiveness has a significant influence on the blade temperature. With a rising density ratio, the film cooling effectiveness likewise increases, providing an enhanced external cooling of the blade downstream of the film cooling row. This effect was also shown by (Narzary et al., 2011). As expected, the temperature of the uncooled trailing edge is not affected by changes in density ratio, due to the low influence of the cooling there (cf. Figure 2).

Improvements in effectiveness due to film cooling

In the following section, we use CFD simulations to distinguish between the influence of film cooling and convective cooling respectively. For the evaluation of a convectively cooled reference blade, the mass flow through the film cooling holes is set to zero. Then the cooling is evaluated on the basis of the overall cooling effectiveness

$$\varepsilon = \frac{T_{\rm HG} - T_M}{T_{\rm HG} - T_C},\tag{7}$$

where T_M is the blade material temperature, T_{HG} the mainstream temperature at the inlet section and T_C the inlet coolant temperature. To separate the effect of film cooling, the effectiveness difference

$$\Delta \varepsilon := \varepsilon_{\text{film}} - \varepsilon_{\text{conv}} = \frac{T_{M,\text{film}} - T_{M,\text{conv}}}{T_{\text{HG}} - T_{C}}$$
(8)

is used. Figure 8 illustrates the difference in overall cooling effectiveness at comparable boundary conditions for different coolant mass ratios MR. The black line in the graph shows the same operating point as in Figure 7. Three regions can be differentiated following Ornano and Povey (2020). First, the region close to the film cooling row ($s/L \le 0.5$) where the film is substantially unmixed; second, the intermediate region (0.5 < s/L < 1) and third, the region of the uncooled trailing edge ($s/L \ge 1$), where the film cooling jets are fully mixed out.

As expected, there is a notable improvement in cooling effectiveness downstream of the film cooling holes in the first region. When the momentum ratio increases however, the improvement gets smaller until the delta effectiveness becomes negative at very high momentum ratios, signifying that the temperature is higher than for the only convectively cooled blade. It is likely that this occurs as a result of the detachment of the cooling jet, which allows hot gas to reach the blade surface and increases the heat transfer coefficient on the blade surface.

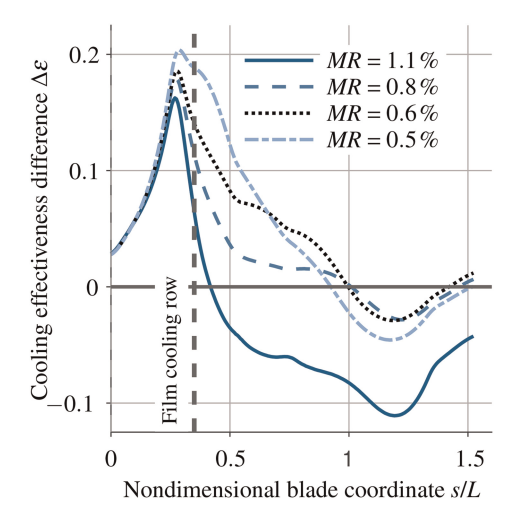


Figure 8. Cooling effectiveness difference $\Delta \varepsilon$ between the film-cooled and an convective-cooled blade.

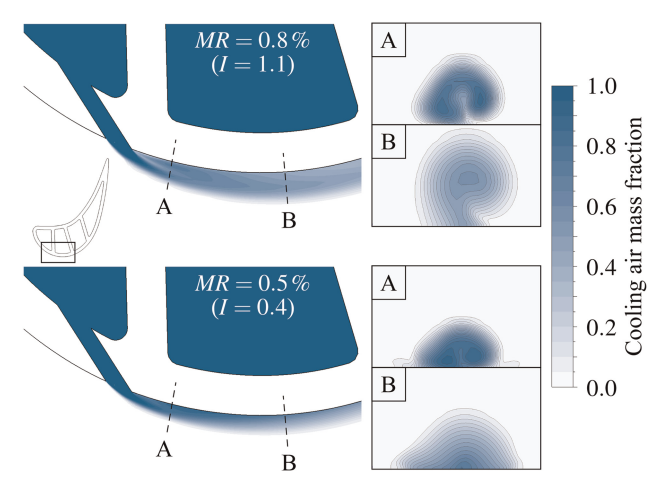


Figure 9. Cooling air mass fraction of the film cooling jets in the middle plane at two positions perpendicular to the jet at two different MR.

Figure 9 shows contours of the cooling air mass fraction in order to visualize the propagation and structure of the film cooling jet entering the external flow. For the higher momentum ratio of I=1.1, the film cooling jet becomes wider, indicating detachment from the blade surface. This is confirmed in the detailed views A and B oriented perpendicular to the jet. For the low momentum ratio of I=0.4 the cooling air is close to the wall. As the momentum ratio increases, the core of the jet detaches from the wall, resulting in a decreasing cooling effectiveness.

In the intermediate region, the effects are more complicated. The reference mass flow ratio (MR = 0.6%) enhances the blade cooling effectiveness significantly, while both higher and lower MR show a lower effectiveness. A higher film cooling mass flow and therefore a higher heat-storage capacity, is beneficial in this region, as long as the film is close to the surface and does not detach. The blade curvature can be favorable here, as long as the momentum ratio is small enough (Ito et al., 1978).

In the mixed-out region, no significant improvement can be observed. For high and low MR, the effectiveness even decreases, which is most likely due to an increased heat transfer coefficient, while the reference ratio and MR = 0.8% provide enough heat-storage capacity to compensate for this effect.

Conclusion

This work investigates a film-cooled turbine blade in a high-temperature environment of 1,050 K at realistic density ratios of $DR \approx 2$. The results show that as long as the jet remains attached, the blade temperature decreases with increasing film cooling mass flow. Additionally, we observe a positive effect of higher density ratios $DR \geq 2.5$ on both internal and external cooling. This highlights the need to match the density ratio for film cooling experiments. It is important to note that the film cooling and convective cooling parameters cannot be varied independently on account of the experimental setup, so their effects are interdependent. We therefore used simulations to distinguish between the effects of internal cooling and film cooling. Furthermore, our findings show that film cooling can even diminish the cooling effectiveness of the blade in comparison to an internally cooled blade, particularly when the mass flow ratio is excessively high (MR > 0.8%). This phenomenon can be attributed to the separation of the film cooling jet from the blade surface, which results in an increased blade surface temperature. Additionally, the cooling air is no longer available for internal cooling. This phenomenon results in an increase in coolant temperature, which in turn leads to elevated metal temperatures due to a combination of reduced conductive heat transfer within the blade and reduced convective heat transfer within the coolant channel.

In the future, we aim to validate these findings experimentally. To achieve this, we plan to measure a blade of the same design that is cooled solely by convection. This will allow us to identify more precisely the effects which are related to film cooling. On this basis, we aim to investigate the superposition effects of multiple film cooling rows by gradually adding more rows on the suction and pressure sides.

Nomenclature

CAM Cooling air measurement section

CHT Conjugated heat transfer

LHTC Linear High-Temperature Cascade

Greek symbols

 ε Overall cooling effectiveness (–)

κ Isentropic coefficient (–)

μ Dynamic viscosity kg/(m s)

 ρ Density (kg/m³)

Indices

C Coolant

conv Convectively-cooled

film Film-cooled

HG Hot gas

in Inlet

is Isentropic

M Material

out Outlet

t Total

Latin symbols

A Cross section area (m^2)

a Speed of sound (m/s)

DR Density ratio DR = ρ_C/ρ_{HG} (-)

I Momentum flux ratio (–)

L Chord length (m)

 \dot{m} Mass flow (kg/s)

Ma Mach number (–)

MR Coolant mass ratio MR = \dot{m}_C/\dot{m}_{HG} (-)

p Pressure (Pa)

R Specific gas constant (J/(kgK))

Re Reynolds number (–)

s Blade coordinate (m)

Temperature (K)

TCR Total coolant ratio (-)

Funding sources

The investigations were conducted as part of the joint research programme "ECOFlex-turbo KüpLe" in the frame of AG Turbo. The work was supported by the Bundesministerium für Wirtschaft und Klimaschutz (BMWK) as per resolution of the German Federal Parliament under grant number 0324358F. The authors gratefully acknowledge AG Turbo and MAN Energy Solutions SE for their support and permission to publish this paper. The responsibility for the content lies solely with its authors.

Competing interests

Jan Lemmer declares that he has no conflict of interest. Yanik Kleine-Hollenhorst declares that he has no conflict of interest. Viola Dehe declares that she has no conflict of interest. Peter Jeschke declares that he has no conflict of interest. Michael Rabs declares that he has no conflict of interest.

References

- Bacci T., Picchi A., and Facchini B. (2019). Flat plate and turbine vane film-cooling performance with laid-back fan-shaped holes. *International Journal of Turbomachinery, Propulsion and Power.* 4 (2): 14. https://doi.org/10.3390/ijtpp4020014.
- Baldauf S., Schulz A., and Wittig S. (1999). High-resolution measurements of local heat transfer coefficients from discrete hole film cooling. *Journal of Turbomachinery*. 123 (4): 749–757. https://doi.org/10.1115/1.1387245.
- Findeisen E., Woerz B., Wieler M., Jeschke P., and Rabs M. (2017). Evaluation of numerical methods to predict temperature distributions of an experimentally investigated convection-cooled gas-turbine blade. In: Volume 5B: Heat Transfer, GT2017. American Society of Mechanical Engineers. https://doi.org/10.1115/gt2017-64205.
- Goldstein R. J. (1971). Film cooling. Advances in Heat Transfer. 7: 321-379. https://doi.org/10.1016/S0065-2717(08)70020-0.
- Goodwin D. G., Moffat H. K., Schoegl I., Speth R. L., and Weber B. W. (2023). Cantera: an object-oriented software toolkit for chemical kinetics, thermodynamics, and transport processes. https://www.cantera.org.10.5281/zenodo.8137090.
- Hylton L. D., Mihelc M. S., Turner E. R., Nealy D. A., and York R. E. (1983). Analytical and experimental evaluation of the heat transfer distribution over the surfaces of turbine vanes, techreport, NASA, Final Report Detroit Diesel Allison, Indianapolis, IN.
- Ito S., Goldstein R. J., and Eckert E. R. G. (1978). Film cooling of a gas turbine blade. *Journal of Engineering for Power*. 100 (3): 476–481. https://doi.org/10.1115/1.3446382.
- Menter F. R. (1994). Two-equation eddy-viscosity turbulence models for engineering applications. *AIAA Journal*. 32 (8): 1598–1605. https://doi.org/10.2514/3.12149.
- Menter F. R., Langtry R. B., Likki S. R., Suzen Y. B., Huang P. G., and Volker S. (2006). A correlation-based transition model using local variables—part i: model formulation. *Journal of Turbomachinery*. 128 (3): 413. https://doi.org/10.1115/1.2184352.
- Mick Y., Wörz B., Findeisen E., Jeschke P., and Caspary V. (2013). Study on relevant effects concerning heat transfer of a convection cooled gas turbine blade under realistic engine temperature conditions. In: Volume 3B: Heat Transfer, GT2013. American Society of Mechanical Engineers. https://doi.org/10.1115/gt2013-94185.
- Narzary D. P., Liu K.-C., Rallabandi A. P., and Han J.-C. (2011). Influence of coolant density on turbine blade film-cooling using pressure sensitive paint technique. *Journal of Turbomachinery*. 134 (3): 1–10. https://doi.org/10.1115/1.4003025.
- Nealy D. A., Mihelc M. S., Hylton L. D., and Gladden H. J. (1984). Measurements of heat transfer distribution over the surfaces of highly loaded turbine nozzle guide vanes. *Journal of Engineering for Gas Turbines and Power*. 106 (1): 149–158. https://doi.org/10.1115/1.3239528.
- Okamura T., Kawagishi H., Koga A., and Itoh S. (2003). Evaluation tests of 1700 °C class turbine cooled blades for a hydrogen fueled combustion turbine system. *Heat Transfer—Asian Research*. 32 (3): 237–252. https://doi.org/10.1002/htj.10088.
- Ornano F. and Povey T. (2020). Theory of non-dimensional groups in film effectiveness studies. *Journal of Turbomachinery*. 142 (4): 1–20. https://doi.org/10.1115/1.4046277.
- Pei Y., Mehl M., Liu W., Lu T., Pitz W. J., and Som S. (2015). A multicomponent blend as a diesel fuel surrogate for compression ignition engine applications. *Journal of Engineering for Gas Turbines and Power*. 137 (11): 1–9. https://doi.org/10.1115/1.4030416.
- Rådeklint U. R. and Hjalmarsson C. S. (1998). A new test facility for testing of cooled gasturbine components. In: Volume 2: Aircraft Engine; Marine; Microturbines and Small Turbomachinery, GT1998. American Society of Mechanical Engineers. https://doi.org/10.1115/98-gt-557.
- Ramesh S., Ekkad S. V., Straub D. L., Lawson S. A., and Alvin M. A. (2014). Experimental and computational analysis of film cooling hole performance on a high temperature test rig. In: Volume 8B: Heat Transfer and Thermal Engineering, IMECE2014. American Society of Mechanical Engineers. https://doi.org/10.1115/imece2014-38735.
- Rubensdörffer F. G. and Hjalmarsson C. S. (1998). Experimental and numerical investigation of heat transfer on a cooled turbine vane. In: Volume 4: Heat Transfer; Electric Power; Industrial and Cogeneration, GT1998. American Society of Mechanical Engineers. https://doi.org/10.1115/98-gt-212.
- Rutledge J. L., Polanka M. D., and Greiner N. J. (2016). Computational fluid dynamics evaluations of film cooling flow scaling between engine and experimental conditions. *Journal of Turbomachinery*. 139 (2): 1–7. https://doi.org/10.1115/1.4034557.
- Turner A. B. (1971). Local heat transfer measurements on a gas turbine blade. *Journal of Mechanical Engineering Science*. 13 (1): 1–12. https://doi.org/10.1243/jmes_jour_1971_013_003_02.
- Wallin S. and Johansson A. V. (2000). An explicit algebraic reynolds stress model for incompressible and compressible turbulent flows. Journal of Fluid Mechanics. 403: 89–132. https://doi.org/10.1017/s0022112099007004.